Dynamic neutron imaging of solute transport and fluid flow in sandstone before and after mineral precipitation

Paiman Shafabakhsh[1], Benoit Jérome Bertrand Cordonnier[2], Anne Pluymakers[3], Tanguy Le Borgne[4], Joachim Mathiesen[5], Gaute Linga[1], Yi Hu[1], Anders Kaestner[6], and François Renard[1]

[1]University of Oslo
[2]ETH Zürich
[3]Delft University of Technology
[4]Université de Rennes 1
[5]Niels Bohr Institute, University of Copenhagen
[6]Paul Scherrer Institut (PSI)

September 30, 2023

Abstract

Advances in micro-scale imaging techniques, such as X-ray microtomography, have provided new insights into a broad range of porous media processes. However, direct imaging of flow and transport processes remains challenging due to spatial and temporal resolution limitations. Here, we investigate the use of dynamic three-dimensional neutron imaging to image flow and transport in Bentheim sandstone core samples before and after in-situ calcium carbonate precipitation. First, we demonstrate the applicability of neutron imaging to quantify the solute dispersion along the interface between heavy water and a cadmium aqueous solution. Then, we monitor the flow of heavy water within two Bentheim sandstone core samples before and after a step of in-situ mineral precipitation. The precipitation of calcium carbonate is induced by reactive mixing of two solutions containing CaCl2 and Na2CO3, either by injecting these two fluids one after each other (sequential experiment) or by injecting them in parallel (co-flow experiment). We use the contrast in neutron attenuation from time-lapse tomograms to derive three-dimensional fluid velocity field by using an inversion technique based on the advection-dispersion equation. Results show mineral precipitation induces a wider distribution of local flow velocities and leads to alterations in the main flow pathways. The flow distribution appears to be independent of the initial distribution in the sequential experiment, while in the co-flow experiment, we observed that higher initial local fluid velocities tended to increase slightly following precipitation. These findings suggest that neutron imaging is a promising technique to investigate dynamics processes in porous media.

Hosted file

`974246_0_art_file_11394007_s14xz5.docx` available at https://authorea.com/users/667035/articles/667546-dynamic-neutron-imaging-of-solute-transport-and-fluid-flow-in-sandstone-before-and-after-mineral-precipitation

Hosted file

`974246_0_supp_11394009_s14s6f.docx` available at https://authorea.com/users/667035/articles/667546-dynamic-neutron-imaging-of-solute-transport-and-fluid-flow-in-sandstone-before-and-after-mineral-precipitation

Dynamic neutron imaging of solute transport and fluid flow in sandstone before and after mineral precipitation

Paiman Shafabakhsh[1, *], Benoît Cordonnier[1], Anne Pluymakers[2], Tanguy Le Borgne[1,3], Joachim Mathiesen[1,4], Gaute Linga[1], Yi Hu[1], Anders Kaestner[5], François Renard[1,6]

[1] The Njord Centre, Departments of Geosciences and Physics, University of Oslo, Norway

[2] Civil Engineering and Geosciences, TU Delft, The Netherlands

[3] Geosciences Rennes, Université de Rennes 1, France

[4] Niels Bohr Institute, University of Copenhagen, Denmark

[5] Laboratory for Neutron Scattering and Imaging, Paul Scherrer Institute, Switzerland

[6] ISTerre, Université Grenoble Alpes, Université Savoie Mont Blanc, CNRS, IRD; Université Gustave Eiffel, 38000 Grenoble, France

[*] Correspondence: paimans@uio.no

Key Points:

- Dynamic neutron imaging is used to image flow and transport in porous rock and investigate the effect of carbonate precipitation
- The velocity field of injected fluid is estimated by solving the advection-dispersion equation using the contrast in neutron attenuation
- Carbonate precipitation widens the distribution of fluid velocities due to local pore-clogging

Abstract

Advances in micro-scale imaging techniques, such as X-ray microtomography, have provided new insights into a broad range of porous media processes. However, direct imaging of flow and transport processes remains challenging due to spatial and temporal resolution limitations. Here, we investigate the use of dynamic three-dimensional neutron imaging to image flow and transport in Bentheim sandstone core samples before and after in-situ calcium carbonate precipitation. First, we demonstrate the applicability of neutron imaging to quantify the solute dispersion along the interface between heavy water and a cadmium aqueous solution. Then, we monitor the flow of heavy water within two Bentheim sandstone core samples before and after a step of in-situ mineral precipitation. The precipitation of calcium carbonate is induced by reactive mixing of two solutions containing $CaCl_2$ and Na_2CO_3, either by injecting these two fluids one after each other (sequential experiment) or by injecting them in parallel (co-flow experiment). We use the contrast in neutron attenuation from time-lapse tomograms to derive three-dimensional fluid velocity field by using an inversion technique based on the advection-dispersion equation. Results show mineral precipitation induces a wider distribution of local flow velocities and leads to alterations in the main flow pathways. The flow distribution appears to be independent of the initial distribution in the sequential experiment, while in the co-flow

experiment, we observed that higher initial local fluid velocities tended to increase slightly following precipitation. These findings suggest that neutron imaging is a promising technique to investigate dynamics processes in porous media.

Keywords: fluid flow, porous rock, calcium carbonate precipitation, neutron and X-ray microtomography

1. Introduction

The transport and mixing of reactive fluids through porous media can modify the porosity structure in geological systems (e.g., Baqer and Chen, 2022; Hommel et al., 2018; Kudrolli and Clotet, 2016). A prime example is porosity reduction and clogging due to mineral precipitation (e.g., Dávila et al., 2020; Emmanuel and Berkowitz, 2005), which is commonly observed in the sealing of faults and fractures by pore fluids (e.g., Fisher and Knipe, 1998), microbial activity leading to bio-clogging (Thullner et al., 2002), as well as in industrial applications, such as effluent disposal (Eriksson and Destouni, 1997). However, characterizing the interplay between fluid flow transport and mineral precipitation is challenging as it occurs across a broad range of temporal and spatial scales (Bray et al., 2017; Emmanuel and Berkowitz, 2005).

Flow and reactive transport in porous rocks are often considered at the continuum scale (Lichtner, 1996), in particular for field applications (e.g., Ebigbo et al., 2012). However, chemical reactions non-linearly change the pore space at scales below the continuum scale, making it challenging to quantify the evolution of porous media (Noiriel and Soulaine, 2021; Sabo and Beckingham, 2021; Seigneur et al., 2019). Non-dimensional numbers can be used as indicators for distinguishing various precipitation patterns and regimes (Hoefner and Fogler, 1988; Steefel and Lasaga, 1990). These include the Péclet (Pe) and Damköhler (Da) numbers which are defined locally as $Pe = \tau_d / \tau_a$ and $Da = \tau_a / \tau_r$, where τ_a, τ_d, and τ_r are the characteristic advection, diffusion, and reaction times, respectively (Hoefner and Fogler, 1988; Steefel and Lasaga, 1990). Since the rate of mineral growth can vary throughout the porous media and over time (Godinho et al., 2016), the effective reaction kinetics are non-trivial (Battiato and Tartakovsky, 2009, 2011).

Among minerals, calcite precipitation ($CaCO_3$) has attracted much attention for its importance in permanent geological storage of CO_2 (e.g., Chang et al., 2017), enhanced oil recovery operations (Wu et al., 2017), geothermal energy recovery (Simmons and Christenson, 1994), and soil stabilization (Mujah et al., 2017). Efforts to understand the kinetics of calcite precipitation have led to the derivation of several rate equations for a range of experimental conditions (Mitchell et al., 2019; Plummer et al., 1979; Zhang and Dawe, 1998). Calcite nucleation and growth at the pore scale depend on several parameters such as pH, temperature, and solute concentration, and require descriptions of coupled processes over a wide range of scales (Noiriel and Soulaine, 2021). Direct imaging of calcite precipitation and solute transport inside porous rocks remains a bottleneck to understand these processes. Since rocks are not transparent to visible light, imaging their interior requires specific techniques that utilize radiations capable of penetrating a rock and providing information about its internal structure.

Recent developments in dynamic imaging techniques at the pore to core scales, such as neutrons and X-rays microtomography with spatial resolutions of a few to tens of micrometers offer unprecedented opportunities for high-resolution continuum monitoring and modeling of reactive transport in porous rocks (e.g., Mancini et al., 2020). In the past twenty years, X-rays have been widely used to obtain high spatial and temporal resolution of three-dimensional microstructures of solid matrix in porous media (e.g., Desrues et al., 2010; Renard et al., 2004). Standard X-ray sources have a much lower attenuation coefficient to water compared to the solid phase of rock; thus, usually, a contrasting agent, such as iodine is used to image the fluid (Andrew et al., 2015; Kim et al., 2013; Scanziani et al., 2020; Vinegar, 1986). Moreover, because X-rays are also adsorbed by the solid matrix, the separation of the fluid from the solid, i.e., the segmentation between these phases, may be challenging. Neutron imaging, on the other hand, is very sensitive to a few elements, including hydrogen and cadmium, allowing imaging of these elements with sufficient contrast, whereas most other elements are almost transparent to neutrons (Anderson et al., 2009). Because neutron imaging is sensitive to hydrogen atoms (protium and deuterium), this technique can image minimal amounts of aqueous water in the pore space, and water contained in hydrated minerals, such as clays (Perfect et al., 2014), without imaging the surrounding solid matrix. Conversely, in the case of heavy water where deuterium replaces both hydrogen atoms, the contrast to neutrons is much lower. Recent advances in neutron imaging technique offer the capability to acquire three-dimensional time series of fluid flow in opaque rocks with acquisition times in the range 5-30 minutes and spatial resolution of several tens of micrometers (Kaestner et al., 2007; Tengattini et al., 2021; Tötzke et al., 2011; Tudisco et al., 2019).

Several laboratory experiments of carbonate precipitation/dissolution in porous media during reactive transport have highlighted the importance of the dynamics of porosity and permeability evolution in both the pore scale and the Darcy scale (Baqer and Chen, 2022; Beckingham, 2017; Garing et al., 2015). Calcite crystal nucleation and growth in model porous media and fractures have been investigated using X-ray microtomography imaging (Noiriel et al., 2021; 2012). Experiments with flow-controlled conditions in a Hele-Shaw cell have been performed to observe various calcite precipitation patterns controlled by different injection flow rates (Balog et al., 2019; Izumoto et al., 2022; Schuszter et al., 2016). While a variety of spatial distributions of calcite minerals leading to porosity and permeability evolution have been observed in previous studies, assessing the impact of mineral precipitation on fluid flow properties inside an intact rock matrix remains an important challenge and requires in-situ data.

The main objectives of this study are to use neutron imaging techniques to study fluid flow in porous sandstone and to quantify how the precipitation of calcite into the porous medium changes the flow and transport properties. Here, we aim to (1) demonstrate the feasibility of neutron imaging to explore the mixing of two miscible aqueous fluids during co-injection into porous sandstone and (2) investigate the impact of calcite precipitation on the fluid velocity distribution in porous rock. We use time-lapse neutron microtomography imaging to track fluids injected into core samples of Bentheim sandstone. Then, we derive the three-dimensional flow velocity field by solving an inverse problem based on the advection-dispersion equation and the contrast in neutron attenuation of the sequential images. Results show that neutron imaging can

be used to measure the variability of flow properties in porous rock and quantify how the flow velocity field is modified after calcite precipitation. We also used X-ray imaging at different resolutions, showing the calcite precipitate distribution inside the rock, although it was not directly comparable to the velocity images since the unconsolidated precipitate was transported by flow between the neutron and X-ray scans.

2. Methods

2.1 Experimental set-up and dynamic three-dimensional imaging

We have performed three flow-through experiments on cylindrical core samples of Bentheim sandstone, 5 cm diameter and 5 cm height, cored perpendicularly to sedimentary bedding from the same block. This reservoir rock contains mainly quartz grains with sizes in the range 200-400 micrometers and the pore sizes are in the range 50-500 micrometers (Klein et al., 2001). The rock has a porosity of 21% and is considered to be homogeneous in the continuum scale. Experiments were performed at the ambient temperature of 24° C. They are labeled BS0 for the fluid tracer test, and BS1 and BS2 for the calcium carbonate precipitation experiments.

We have built core holders made of polytetrafluoroethylene (PTFE) and a jacket of fluorinated ethylene propylene (FEP) surrounds the rock sample within the core holder. Both materials do not contain hydrogen atoms and are therefore almost transparent to neutrons. The core holder contains two inlets connected to a syringe pump injecting fluid at a given flow rate from either the top extremity of the core sample (experiments BS0 and BS1) or its bottom extremity (experiment BS2). An outlet at the opposite side of the core holder collects the fluid after flow-through in the sample and is at atmospheric pressure (Figure 1a). Porous diffusers made of sponge or porous glass were used at the inlets and outlet points to diffuse the fluid, allowing almost homogenous injection and outflow conditions over the circular surface area of the sample. At the inlet side, a barrier separates the two injected fluids in co-flow experiments, preventing their mixing before reaching the sample. The core holder was installed on the rotating stage of the ICON neutron imaging beamline of the SINQ neutron spallation source (Paul Scherrer Institute, Switzerland), with a source neutron flux of 10^{14} n/cm^2/s (Kaestner et al., 2011). A laboratory X-ray tomograph was installed at the Paul Scherrer Institute (Kaestner et al., 2017) and enabled X-ray imaging at different stages of experiment BS2 (Figure 1b).

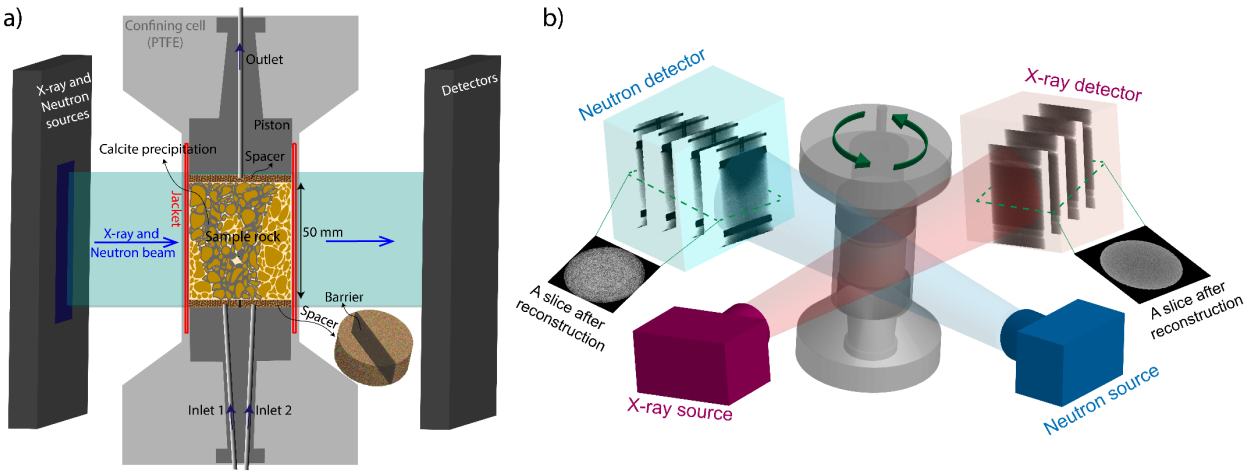

Figure 1: Schematic of the experimental set-up at the ICON beamline at the Paul Scherrer Institute, Switzerland: **a)** Sample rock (5 cm diameter, 5 cm height) inside the core holder with two inlets for fluid co-flow injection and one fluid outlet. Here, the sketch shows injection from the bottom of the core sample, against gravity. Rotating this set-up upside down allows injecting fluids from the top, in the direction of gravity. **b)** Sketch of the rotating core holder on the rotating stage and image acquisition using both neutron and X-ray sources.

Time-lapse neutron three-dimensional tomography images of the rocks were acquired with a voxel size of 62 micrometers, and each radiograph of the samples contained 800×800 pixels. The voxel size is on the same order of magnitude as the mean sandstone pore size (50-200 micrometers) and therefore the neutron measurements are averaged over around one pore size. The three-dimensional tomograms were obtained from 626 projections covering the 360-degree rotation of the core holder, and the average acquisition time of a scan was 32 minutes. The X-ray tomograms acquired at the Paul Scherrer Institute have a voxel size of 32 micrometers with an acquisition time of 75 minutes. The neutron and X-ray volumes were reconstructed with scattering correction using the open-source software MuhRec developed by Kaestner (2011).

Sample BS2 after precipitation was also imaged using X-ray microtomography at the European Synchrotron Radiation Facility, one year after the experiment was performed. This duration was necessary to let the radioactivity of the sample decay sufficiently enough after imaging it with neutrons. During this year, the sample, saturated with heavy water, was stored horizontally in the experimental hutch of the SINQ neutron beamline at the Paul Scherrer Institute. At the European Synchrotron Radiation Facility, we acquired a high-resolution X-ray tomogram of the entire sample on beamline BM18 with a voxel size of 5.85 micrometers, allowing imaging details within pores. Although high-resolution X-ray imaging was useful to verify the presence of calcite precipitate inside the rock, the distribution of unconsolidated precipitate inside the rock was likely affected by the horizontal storage of the sample.

2.2 Flow-through experiments

2.2.1 Fluid mixing test (experiment BS0)

The experiment BS0 is a test to demonstrate the feasibility of three-dimensional time-lapse neutron imaging to study fluid mixing in porous rock. We used two miscible fluids, a solution of deuterium oxide heavy water (D_2O) and a solution of heavy water with dissolved cadmium ($CdCl_2$), an element that provides good contrast for neutron imaging and that was used in a previous study (Cordonnier et al., 2019). After fully flushing the sample with heavy water, we injected heavy water from one inlet at the top of the core sample and 1 M of $CdCl_{2\,(aq)}$ (dissolved in heavy water) from the other inlet at the top. Figure 2 shows the time series of the neutron tomograms during the D_2O and $CdCl_2$ injections. For all experiments, chemicals were provided by Sigma Aldrich.

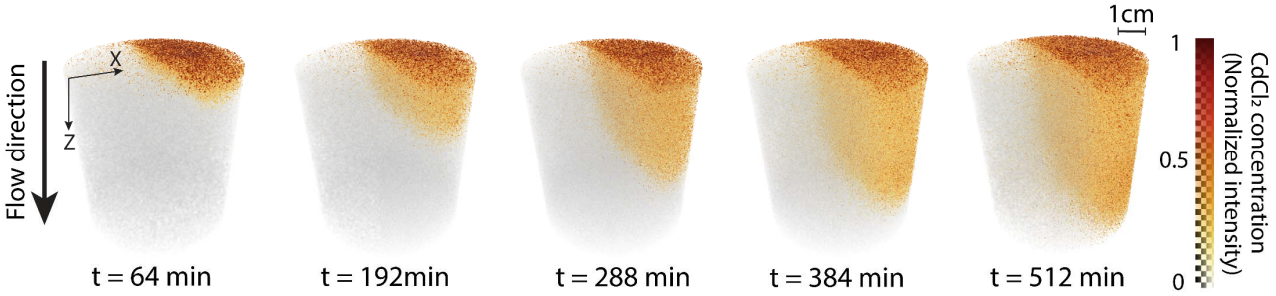

Figure 2: Time series of neutron tomograms acquired during the co-injection and mixing of D_2O (transparent) and $CdCl_2$ (orange color) solutions injected simultaneously from the two inlets at the top of sample BS0 (gray color). Initially, the rock was saturated with D_2O. The time t=0 corresponds to the start of the injection.

With this experiment, we investigate the applicability of neutron imaging to analyze fluid mixing by measuring transverse dispersion in sandstone rock. Assuming that the linear attenuation coefficients of injected fluids are constant through time, we can estimate the concentration of cadmium solution at each voxel of the three-dimensional volume and its relative evolution with time, based on the Beer-Lambert law (Swinehart, 1962). Taking the last scan of this test where the mixture reached a steady state, a $CdCl_2$ solution was injected continuously and formed a plume that extended downward via advection and grew in the lateral dimension through dispersion. Assuming the lateral velocity is small compared to the longitudinal velocity, the transverse dispersion equation for the steady-state plume is:

$$\overline{u_z}\partial_z I = D_T \partial_x^2 I \tag{1}$$

where $\overline{u_z}$ [L/T] is the average downward velocity, I [-] is the normalized gray level intensity at each pixel (i.e., normalized neutron attenuation coefficient), and D_T [L^2/T] is the transverse dispersion, perpendicular to the interface between the two fluids. The solution of Eq. (1) with unbounded boundary conditions is (Gautschi and Cahill, 1964):

$$c(x,z) = \frac{I_1 + I_2}{2} + \frac{I_1 - I_2}{2}\left(\mathrm{erf}\left(\frac{x - z\overline{u_z}}{2\sigma}\right)\right) \tag{2}$$

where I_1 and I_2 are the relative concentrations of the two solutions that correspond in our case to the normalized neutron attenuation coefficient of heavy water and cadmium solutions, and $\sigma = \sqrt{\alpha z}$, where solute dispersivity is defined as $\alpha = D_T / \overline{u_z}$ [L].

2.2.2 Flow prior to and after calcium carbonate precipitation (experiments BS1 and BS2)

The objectives of experiments BS1 and BS2 were to measure and assess the spatial distribution of velocity before and after two different calcite precipitation modes: the two solutions used to precipitate calcite were injected in the sample either one after each other from the same inlet in a sequential mode (experiment BS1), or simultaneously in two inlets in a co-flow mode (experiment BS2). We used several aqueous fluids. Distilled water (H_2O) and heavy water (D_2O) were mixed at different proportions in the preparation of the solutions to control the neutron imaging contrast. The steps of fluid injections in the rocks and the injection flow rates are indicated in Figure 3. The experiment BS1 (injection from the top of the core sample) contained two steps of mineral precipitation, and heavy water was injected before and after the second step (Figure 3a). For experiment BS2 (injection from the bottom), one step of mineral precipitation was performed with heavy water injections before and after this step (Figure 3b). For the heavy water injections, the characteristic advection time is approximated as $\tau_a = L/v = 100\ s$, where $L = 200\ \mu m$ is the pore size, $v = 2\times10^{-6}\ m/s$ is the fluid velocity. The characteristic diffusion time is approximated as $\tau_d = L^2/D = 50\ s$ where $D = 7.5\times10^{-10}\ m/s$. Thus, the Péclet number is $Pe = \tau_d/\tau_a = 0.5$. While the characteristic reaction time varies locally within the porous media and changes over time, it is approximated $\tau_r = 5\ s$ by Izumoto et al. (2022), obtained from a millifluidic experiment of calcite formation leading to a Damköhler number $Da = \tau_a/\tau_r = 20$.

The precipitation of calcium carbonate is controlled by the injection of two aqueous solutions containing $CaCl_2$ and Na_2CO_3 at the inlets ($CaCl_{2\ (aq)} + Na_2CO_{3\ (aq)} \rightarrow CaCO_{3\ (s)} + 2NaCl_{\ (aq)}$). Because the precipitation is quasi-instantaneous when the two fluids mix into the rock, several types of calcium carbonate could form, such as amorphous calcium carbonate, vaterite, aragonite, and calcite (Brečević and Nielsen, 1989; Morse et al., 2007). Calcite is the most stable phase under our experimental conditions and therefore should be the dominating mineral at the end of each experiment.

Following a series of calibration tests, similar to the procedure followed by Cordonnier et al. (2019), the combination of 75% heavy water and 25% distilled water was used for the $CaCl_{2\ (aq)}$ solution, and a combination of 25% heavy water and 75% distilled water was used for the Na_2CO_3 solution. These proportions of distilled and heavy water provide good contrast in the neutron images to detect the miscible fluids separately.

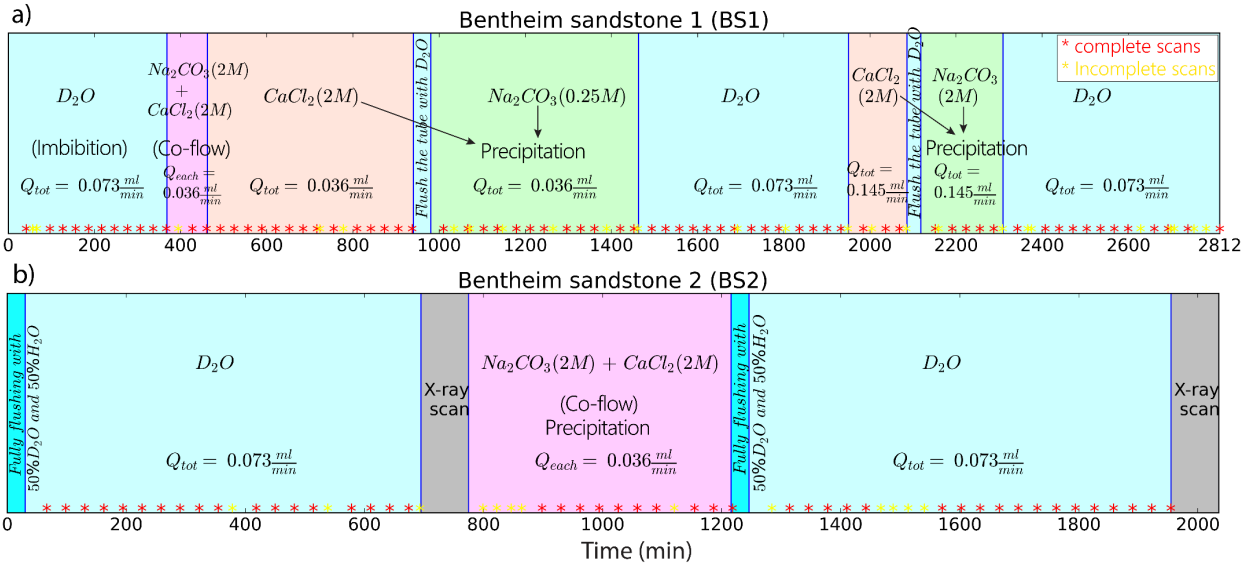

Figure 3: The fluid injection steps of the two mineral precipitation experiments performed on Bentheim sandstone. For experiment BS1 (a), the fluids were injected from the top to the bottom, along the direction of gravity, and for experiment BS2 (b) the injection was from the bottom to the top. Calcium carbonate precipitation was performed by either injecting simultaneously the Na_2CO_3 and $CaCl_2$ solutions in the two inlets of the core holder (co-flow, pink) or by injecting one solution after the other from the same inlet (sequential flow, orange). Short periods where water was injected to flush the tubes and avoid calcium carbonate precipitation in them are also indicated in bright blue. The core samples were imaged with three-dimensional neutron tomography during the main injection steps, and two-dimensional radiographs were acquired during the flushing steps. The red stars on the time axis show the complete neutron tomography scans and the yellow stars indicate incomplete scans (due to camera failure), from which we used two-dimensional radiographs. Due to their longer acquisition time, two X-ray scans were acquired before and after calcium carbonate precipitation for sample BS2.

The initially dry BS1 sample was filled with D_2O at a constant flow rate, with water replacing air (Figure 3a, from 0 to 368 minutes). This imbibition step was followed by a step of injection of $CaCl_{2\ (aq)}$ and $Na_2CO_{3\ (aq)}$ in parallel from the two inlets (co-flow from 368 to 462 minutes). However, the flow stopped due to the clogging of one of the inlet tubes with calcium carbonate precipitates. The experiment was continued as a sequential injection of $CaCl_2$ (from 462 to 940 minutes) and then Na_2CO_3 (from 940 to 1463 minutes) solutions successively from the same inlet. After these steps, we injected D_2O to measure the fluid velocity distribution. Then, two successive steps of sequential injections of $CaCl_2$ (from 1950 minutes to 2086 minutes) and Na_2CO_3 (from 2118 minutes to 2309 minutes) induced a second episode of precipitation before another step of D_2O injection was performed. During experiment BS1, we experienced some failures of the camera of the neutron tomograph, which resulted in some incomplete scans indicated as yellow stars on the time axis in Figure 3. The duration of this experiment was 47 hours.

We performed a second experiment with calcium carbonate precipitation on sample BS2 (Figure 3b). Here, we injected the fluids from the bottom of the sample. Before the experiment, the sample was saturated with water. We first fully flushed the sample (~ two pore volumes)

with a mixture of 50% of D_2O and 50% of H_2O. Then, we injected D_2O, (from 30 minutes to 695 minutes) to measure the fluid velocity distribution. Then, we performed a co-flow injection of the two reactive solutions from the two inlets for an episode of calcium carbonate precipitation (from 775 minutes to 1216 minutes), and then a final injection of D_2O (from 1246 minutes to 1955 minutes) to measure the velocity distribution after precipitation. In the course of the co-flow injection of $CaCl_2$ and Na_2CO_3, we experienced clogging of the tubes due to the formation of calcium carbonate precipitates in the porous media that redirected the flow of one solution toward the other. Therefore, this co-flow experiment was unsteady and effectively consisted of a series of injections of one and the other solution as the tube alternatively clogged and unclogged. These side flows and pre-mixing before the injection into the rock contributed to a less homogeneous distribution of precipitation within the rock. This was interesting to test the flow imaging method in a heterogeneous sample. Two X-ray scans were acquired when the rock was saturated with D_2O, one before and one after the precipitation phase. The second X-ray was subsequent to the final D_2O injection, and this additional flow likely altered the unconsolidated precipitate distribution during the D_2O injection process. The duration of this experiment was 34 hours.

2.3 Calculation of the flow velocity field

The distinctive grayscale levels of the various miscible fluids utilized in our study enable us to identify and track the interface between them over time. The interface is seen as a strong gradient in the intensity of the neutron tomograms. Due to imposed fluid flow conditions, the interface is transported mainly in the direction of the cylindrical core axis. In order to compute the velocity of the interface, we solve an inverse problem based on the advection-dispersion equation by using the contrast in neutron attenuation between different fluids from time-lapse tomograms. The advection-dispersion equation is:

$$\varphi\frac{\partial I}{\partial t}+\nabla.(I\mathbf{u})=\nabla.(D\nabla I) \tag{3}$$

where φ [-] is the porosity, I [-] is the normalized gray level intensity at each pixel, t [T] is the time between two consecutive tomograms, $\vec{\mathbf{u}}=(u,v,\omega)$ [L/T] is the fluid velocity, and D [L^2/T] is a dispersion coefficient. Defining the velocity vector $\vec{\mathbf{u}}^*=(u^*,v^*,\omega^*)$ as

$$\mathbf{u}^*=\mathbf{u}-D\frac{\nabla I}{I} \tag{4}$$

allows deriving the three-dimensional velocity field of the injected heavy water by tracking how the interface between heavy water and distilled water moves through the sample. The path-averaged velocity of fluid transported by advection only is calculated by:

$$\varphi\frac{\partial I}{\partial t}+\vec{\mathbf{u}}^*.\nabla I=0 \tag{5}$$

where $\vec{\mathbf{u}}^*$ is the velocity field transported by advection at each voxel. We have combined this advection equation with a global smoothness term to constrain the estimated velocity field (Horn and Schunck, 1981) by minimizing the function:

$$J_{(u,v,\omega)} = \int_{\Omega}\left[\varphi\frac{\partial I}{\partial t} + \vec{\mathbf{u}}^{*}.\nabla I\right]^2 dxdydz + \lambda\int_{\Omega}\left[\left|\nabla u^{*}\right|^2 + \left|\nabla v^{*}\right|^2 + \left|\nabla \omega^{*}\right|^2\right] dxdydz \quad (6)$$

where Ω is the domain of the three-dimensional volume, and λ is a Lagrange multiplier to smooth out the sharp velocity changes. There is no rigorous methodology for determining the Lagrange multiplier in the variational formulation; however, the solution of this equation remains relatively insensitive to the value of λ within a broad range (Liu, 2017). We used a value λ=50 empirically selected as suggested by Liu and Shen (2008). As shown in Figure S1, modifying λ in the range 10-50 does not have a significant impact on the velocity distribution, and when λ is larger, the variation will be smoothed out. We calculated the generalized form of the corresponding Euler-Lagrange equation proposed by Horn and Schunck (1981) to minimize $J_{(u^{*},v^{*},\omega^{*})}$ and obtain the velocity field. The iterative numerical solution for the convergence is:

$$\begin{aligned}
u^{*n+1} &= \overline{u^{*n}} - \frac{I_x\left(I_x\overline{u^{*n}} + I_y\overline{v^{*n}} + I_z\overline{\omega^{*n}} + I_t\right)}{\lambda^2 + I_x^2 + I_y^2 + I_z^2} \\
v^{*n+1} &= \overline{v^{*n}} - \frac{I_y\left(I_x\overline{u^{*n}} + I_y\overline{v^{*n}} + I_z\overline{\omega^{*n}} + I_t\right)}{\lambda^2 + I_x^2 + I_y^2 + I_z^2} \\
\omega^{*n+1} &= \overline{\omega^{*n}} - \frac{I_z\left(I_x\overline{u^{*n}} + I_y\overline{v^{*n}} + I_z\overline{\omega^{*n}} + I_t\right)}{\lambda^2 + I_x^2 + I_y^2 + I_z^2}
\end{aligned} \quad (7)$$

where I_x, I_y, I_z are intensity derivatives, and $\overline{u}^{n}$, $\overline{v}^{n}$, $\overline{\omega}^{n}$ are averages of the velocity at each voxel of 4×4×4 neighborhood voxels at iteration n. We use a maximum of 50 iterations to obtain the solution, and the iteration stops when the flow field has converged, i.e., when

$$\left\|\vec{\mathbf{u}}^{*n} - \vec{\mathbf{u}}^{*n-1}\right\| \le \mathrm{TOL} \quad (8)$$

at iteration n, where TOL is the tolerance level chosen here equal to 10^{-9} m/s.

To obtain the velocity field $\vec{\mathbf{u}} = (u, v, \omega)$ transported by both advection and dispersion, we use Eq. 4 multiplied by a weighting function $W = |\nabla I|$ as $\vec{\mathbf{u}}^{*}$ includes a contribution from the gradient of intensity. Therefore, the actual velocity field can be derived by solving the set of equations:

$$\left.\begin{aligned}
\int Wu^{*}dt &= \int Wudt - D\int W\frac{I_x}{I}\,dt \\
\int Wv^{*}dt &= \int Wvdt - D\int W\frac{I_y}{I}\,dt \\
\int W\omega^{*}dt &= \int W\omega dt - D\int W\frac{I_z}{I}\,dt
\end{aligned}\right\} \rightarrow u, v, \omega \quad (9)$$

where the dispersion coefficient D is approximated by calculating the divergence of Eq. 10 and considering mass conservation ($\nabla.\vec{\mathbf{u}} = 0$) as

$$D = \frac{\left\| \nabla.\vec{\mathbf{u}^*} \right\|}{\left\| \nabla.\left(\frac{\nabla I}{I} \right) \right\|} \tag{11}$$

3. Results

3.1. Fluid mixing during co-injection of water and a cadmium solution (experiment BS0)

This fluid mixing test is conducted to measure transverse dispersivity from neutron images. Figure 4a displays the last scan of the neutron tomogram series following the mixing of D_2O and $CdCl_2$ shown in Figure 2. Slices at some selected heights of this three-dimensional volume are shown in Figure 4b. The top slices of the rock exhibit a distinct sharp interface between D_2O and $CdCl_2$ solutions. As the fluids move toward the lower part of the sample, this sharp interface becomes more diffuse and widen owing to lateral dispersion. Figure 4c presents a series of normalized neutron attenuation profiles along the *x*-direction (perpendicular to the interface and the axis of the sample) at different heights in the sample. Each curve in Figure 4c is plotted along 45 mm in the *x*-direction where each point is calculated by averaging 20×20 voxels in the *yz*-plane and covers the central area (along the *y*-axis) of the slices at several heights *z*. By comparing the curves obtained from the upper (z = 7 mm) and lower (z = 42 mm) sections of the rock, we observe that the mixing zone has become wider towards the lower part of the sample (Figure 4c) since the change in attenuation with lateral distance has become more gradual. This widening is attributed to the transverse dispersion of solutes within the rock increasing with distance from the inlet.

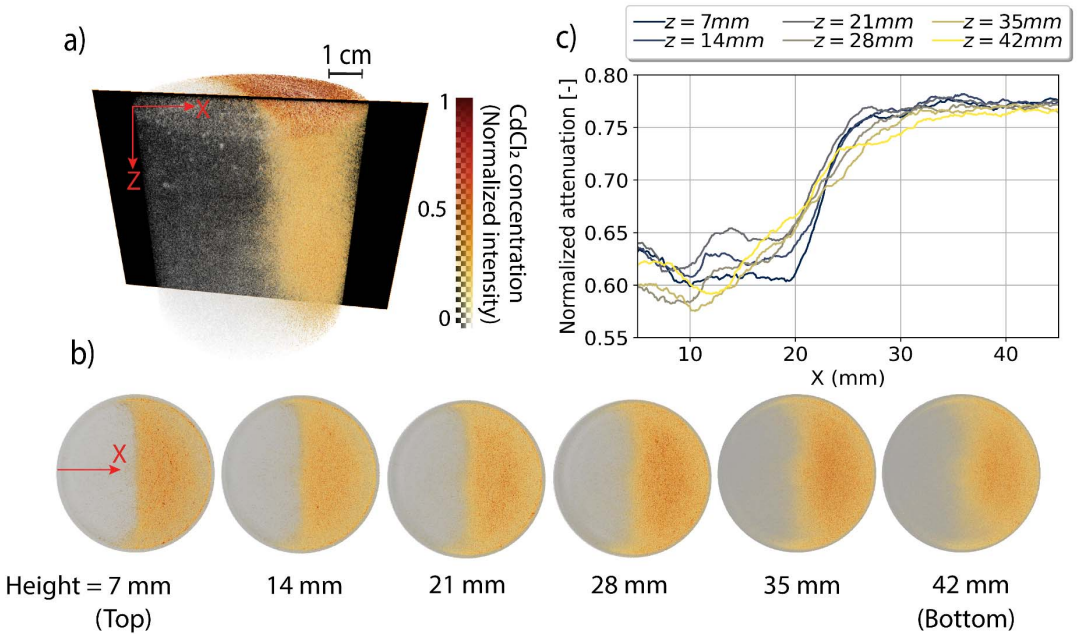

Figure 4: a) Neutron tomogram with a vertical cross-section of the core sample in experiment BS0 after co-flow injection of D_2O and $CdCl_2$. The orange color shows the cadmium solution injected from the right inlet located at the top of the sample while injecting heavy water from the left inlet. **b)** Two-dimensional slices perpendicular to the core axis at different heights. **c)** Normalized attenuation along transects perpendicular to the interface of D_2O and $CdCl_2$ mixing at different heights of sample rock BS0. These lines are calculated as an average of 20 pixels wide transects located at the position of the red arrow in b) and crossing the interface between the two fluids perpendicularly. The broadening of the intensity profiles when crossing the interface between the two fluids from the top (z= 7 mm) to the bottom (z=42 mm) of the sample is due to flow dispersion.

The function described by Eq. 2 can be used to fit the normalized attenuation curves obtained at various heights (Figure 4c). This fitting enables the determination of all the parameters in Eq. 2 including the interface width σ at different heights z. The values obtained are shown in Figure 5. By fitting a square root dependence $\sigma = \sqrt{\alpha z}$ to these data, we estimate the dispersivity $\alpha = 7.0\times10^{-4}\,\mathrm{m}$. Considering the average downward velocity $\overline{u_z} = 1.92\times10^{-6}\,\mathrm{m\ s^{-1}}$ (flow rate divided by the pore area of the surface), we estimate the transverse dispersion coefficient $D_T = \alpha\overline{u_z} = 1.3\times10^{-9}\,\mathrm{m^2 s^{-1}}$. This dispersion coefficient is of the same order of magnitude as the diffusion coefficient of the considered solutes, which is consistent with the considered Pe<1 condition.

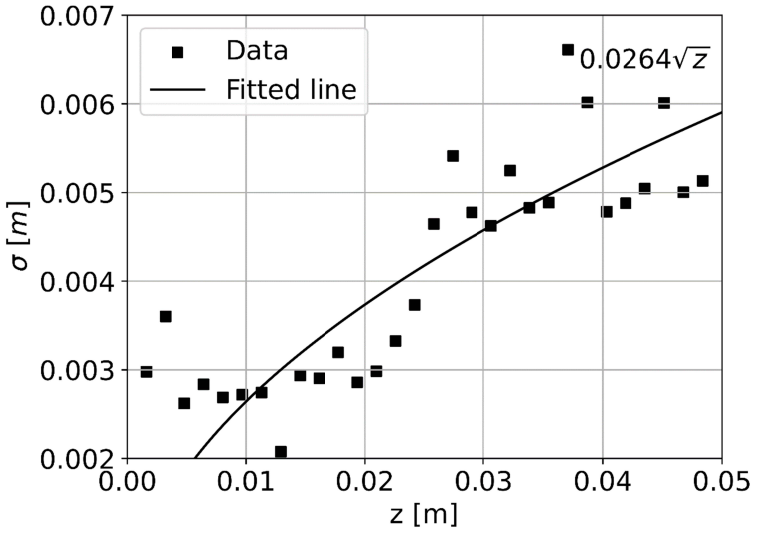

Figure 5: Derived values of interface width σ at different heights *z* in experiment BS0 (filled squares). The solid line shows the best fit of the function $\sigma = \sqrt{\alpha z}$ to the data, which allows us to estimate the dispersivity α. Injection of the two fluids occurs at the height z = 0.

3.2. Fluid velocity distribution before and after calcium carbonate precipitation (experiments BS1 and BS2)

The difference in neutron absorption and scattering cross-sections between D_2O and the initial fluid inside the samples (mixture of D_2O, H_2O, and different solutes) is used to image the flow of D_2O. Figure 6 and Figure *7* show the time series of the neutron tomograms during the

injection of D_2O into samples BS1 and BS2 before and after calcite precipitation. The boundary separating the two aqueous solutions is visible but is not a sharp front due to the dispersion occurring within the interface of the fluids. It should also be noted that the exposure time needed to image the flow interface during injection may blur the moving front in the three-dimensional images; however, injecting with a low flow rate helped reduce this effect. Visual comparison in Figure 6 and Figure *7* indicates dissimilarities in the shape and the velocity of the front progression before and after mineral precipitation. This suggests that calcium carbonate precipitation modified flow pathways in both samples.

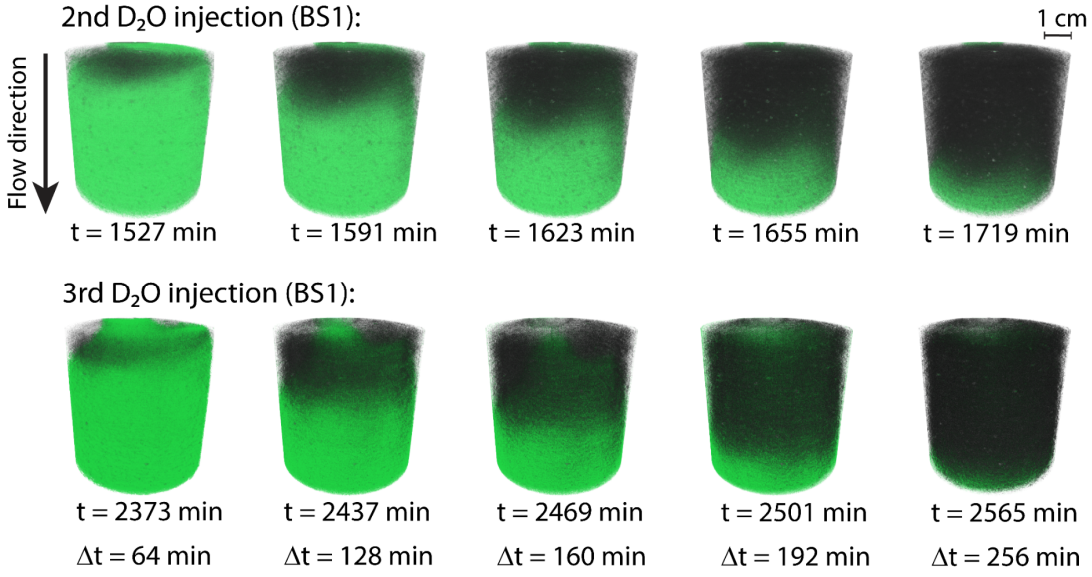

Figure 6: Neutron tomograms during injection of D_2O (dark color) from the top with flow rate 0.073 ml/min into sample BS1. Prior to each injection, the rock was saturated with the calcium carbonate growth solution (Na_2CO_3 and $CaCl_2$), which contained a 25%-75% mixture of D_2O and H_2O (green color). Times *t* correspond to those indicated in Figure 3a, and Δt is the time since the beginning of each injection step.

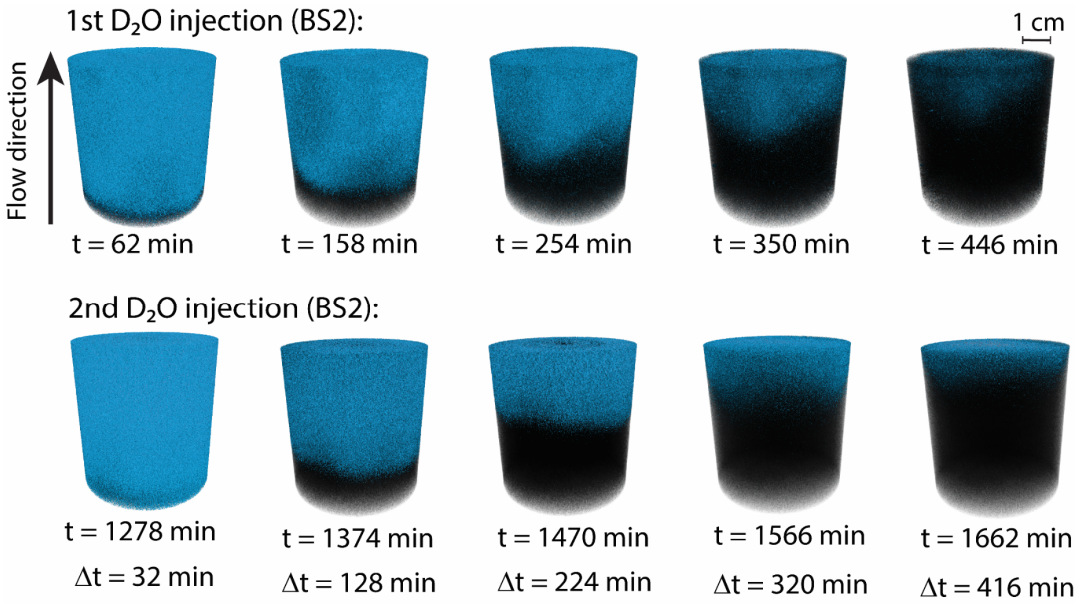

Figure 7: Neutron tomograms during injection of D_2O (dark color) from the bottom with flow rate 0.073 ml/min into sample BS2. Before injection, the rock was saturated with a 50%-50% mixture of D_2O and H_2O (blue color). Times correspond to those indicated in Figure 3b, and Δt is the time since the beginning of each injection step.

The front progression of the injected D_2O in the neutron tomograms allows the velocity distribution of the flow in samples BS1 and BS2 to be calculated using the inversion method based on the advection-dispersion equation (Eq. 3 and section 2.3). Figure 8a shows the probability density function of the derived velocity fields of D_2O flow in sample BS1. Note that these velocities correspond to coarse-grained velocity averaged over the neutron image pixel size and are therefore not measured at the pore scale. The fluid velocity magnitude at three horizontal cross-sections of the second D_2O injection (before the second step of calcium carbonate precipitation) and the third D_2O injection (after the second step of calcium carbonate precipitation) is shown in Figure 8b. Comparing these slices shows the areas where fluid velocity is reduced or increased after local mineral precipitation. We observe that the flow heterogeneity experiences a slight increase following the precipitation.

The probability density function of the velocity magnitude for D_2O injection before precipitation (Figure 8a) shows a fluid velocity range of 0.14-0.26 mm/min and a mean value of 0.19 mm/min. This value is in agreement with a velocity of 0.18 mm/min calculated from the injected flow rate of 0.073 ml/min and the available pore area of the surface (412 mm^2 surface area of the horizontal cross-section of the rock multiplied by the porosity equal to 21%). After precipitation, the mean value of fluid velocity is 0.20 mm/min. Comparing the second and third D_2O injections shows that, for the same flow rate, the average fluid velocity after this step of precipitation is higher than before it, consistent with porosity reduction due to mineral precipitation. We also note that mineral precipitation is associated with a widening of the velocity distribution.

For sample BS2, Figure 9 shows the fluid velocity magnitude of D_2O injections before and after mineral precipitation and the probability density functions of fluid velocity. Before precipitation, the average fluid velocity is 0.14 mm/min, and after precipitation, it is 0.16 mm/min. The velocity magnitude images in Figure 9b show that the central part of sample BS2 hosts lower fluid velocities after precipitation in comparison to the sides of the core sample. We observe that the enhancement in flow heterogeneity is more visible in BS2 than in BS1. The probability density functions of fluid velocity (Figure 9a) clearly show the influence of mineral precipitation between the two injections of D_2O. Similar to the results obtained for sample BS1, fluid flow in sample BS2 shows a higher average velocity and a wider range of fluid velocities after a step of calcium carbonate precipitation.

In the calculation of the velocity field, we assume that the estimated dispersion coefficient deriving from Eq. 11 is constant during each injection. While this assumption appears somewhat restrictive, we verified that the estimated values of D are nevertheless too small to significantly influence the velocity distributions. The derived values of dispersion coefficient D are equal to 5.6×10^{-11} and $9.3\times10^{-11}\,\mathrm{m^2/s}$ for the second and third D_2O injections into BS1. For the first and second D_2O injections into BS2, the values are 8.0×10^{-11} and $3.4\times10^{-10}\,\mathrm{m^2/s}$, respectively.

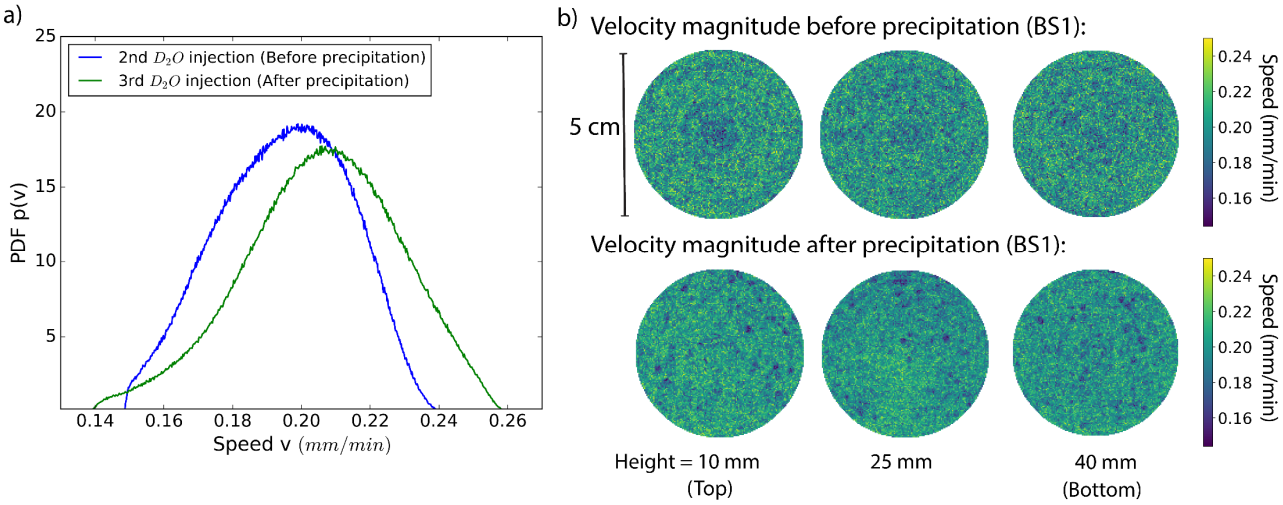

Figure 8: a) Probability density functions of fluid velocity magnitude during two injections of D_2O (2^{nd} and 3^{rd} D_2O injections) in sample BS1. The second injection (blue curve) was performed before the second step of calcium carbonate precipitation (Figure 3a) and the third one (green curve) after it. **b)** Cross-sections perpendicular to the core axis at different heights of local fluid velocities (Eq. 3) before and after the second step of mineral precipitation.

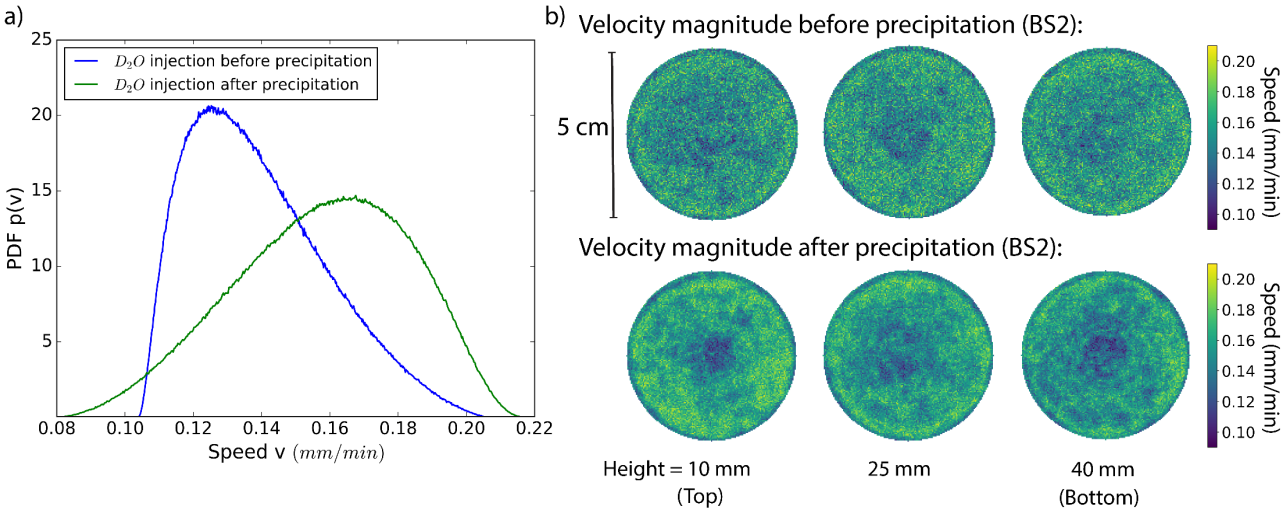

Figure 9: **a)** Probability density functions of fluid velocity magnitude during the injections of D_2O in sample BS2, before (blue curve) and after (green curve) calcium carbonate precipitation. **b)** Cross-sections perpendicular to the core axis at different heights of local fluid velocities before and after the mineral precipitation.

Figure 10a and Figure **10**b display scatter plots illustrating how local fluid velocities after a precipitation step, compare to local velocities before the precipitation step for samples BS1 and BS2, respectively. In the case of BS1, where the precipitation step occurred through sequential injections, there is no correlation between these velocities, suggesting more random changes in the velocity field in response to the precipitation event. For sample BS2, where precipitation was induced by unsteady co-flow injections, we observe a slight positive correlation, where higher initial velocities tend to further increase following precipitation. This observation is substantiated by measuring the average velocity after precipitation as a function of the initial velocities, as shown by the red line along with the variance in the same figure. In the case of BS1, we observe a consistent average velocity after precipitation. However, for sample BS2, there exists an upward trend, signifying a positive correlation. This highlights the distinct behavior exhibited by these two samples in response to the precipitation event.

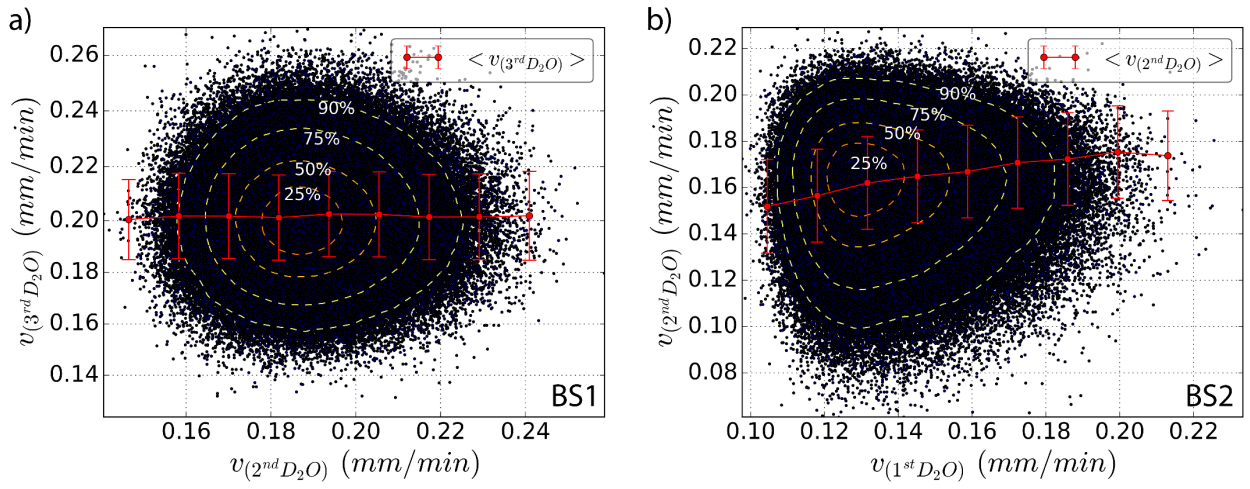

Figure 10: Scatter plots depict the local velocity after a precipitation step in relation to the velocity before the precipitation step for samples BS1 (a) and BS2 (b). Each black dot corresponds to one voxel in the neutron tomogram. Percentages and dashed contours indicate the density of the data. The red line indicates the average post-precipitation velocity at a given initial velocity, along with the variance.

3.3. X-ray microtomography imaging

For experiment BS2, we have acquired two X-ray tomography scans at the Paul Scherrer Institute, one before and one after mineral precipitation. Figure 11a shows the difference between these two scans, displaying the areas where calcium carbonate precipitate appeared. Note, however, that some unconsolidated precipitate likely moved during the heavy water injection. Instead of a straight plane of precipitation in the middle of the rock, which would be expected for a steady co-flow mixing experiment, we observe a complex region of precipitation likely due to the unsteady injection of $CaCl_2$ and Na_2CO_3. The amount of precipitation is higher at the bottom near the inlet points where the solutions of $CaCl_2$ and Na_2CO_3 were injected and also at the top where the calcium carbonate precipitates accumulated at the outlet. Some precipitation occurred in the middle of the sample; however, the resolution of the scans was too low to observe details. Figure 11b shows the average of the difference of gray values after and before mineral precipitation (X-ray attenuation coefficients) along the height of the sample BS2. The curve demonstrates a sharp variation in density near both the inlet and outlet points. We also see increased X-ray adsorption due to the precipitation of calcium carbonate in the center part of the sample, albeit slightly less pronounced than near the inlet/outlet regions.

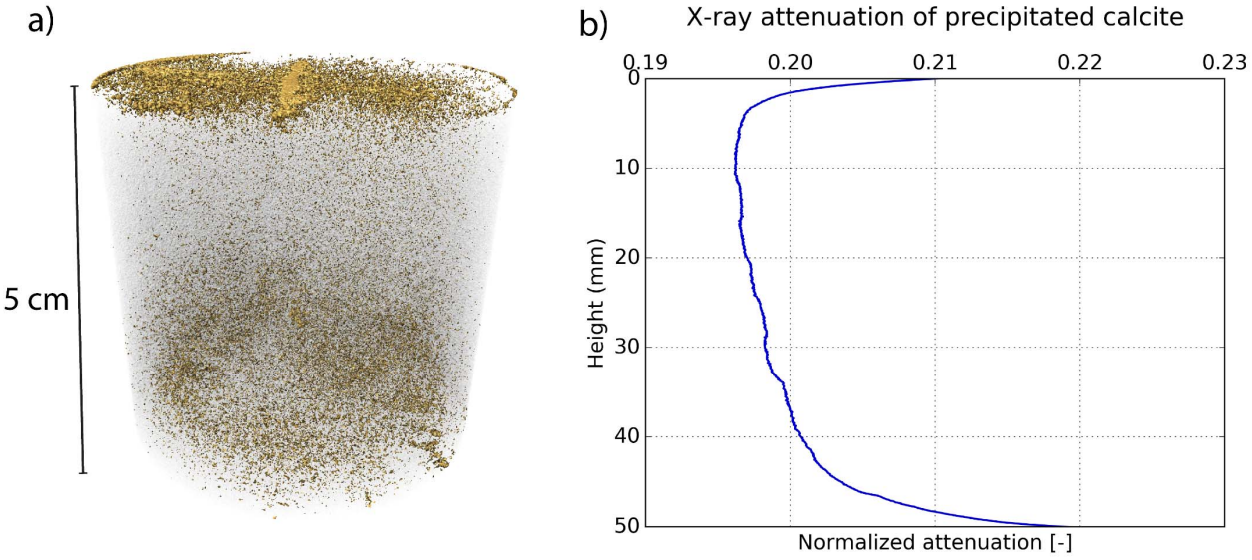

Figure 11: a) X-ray tomography three-dimensional rendering of precipitation of calcium carbonate in sample BS2 acquired at the Paul Scherrer Institute. The image was produced by subtracting the X-ray tomogram after precipitation from the X-ray tomogram before precipitation. **b)** Effect of calcium carbonate precipitation: The differential X-ray attenuation profile along the axis of the core sample is calculated by subtracting the three-dimensional volume after precipitation from the three-dimensional volume before precipitation and averaging along the axis of the core sample.

Segmentation of the pore space in the high-resolution three-dimensional tomogram acquired at the European Synchrotron Radiation Facility shows the porosity after precipitation (Figure 12a). Figure 12b displays four selected slices perpendicular to the axis of the core sample, at different heights. The pores appear in dark gray because of low X-ray adsorption, while the rock grains and precipitates have lighter gray colors. Figure 12c shows the profile of porosity along the height of the core derived from pore segmentation, which we calculate as the summation of segmented pores' surface area divided by the slice surface area along the axis of the core sample. Porosity at both the top and bottom regions of the rock sample is lower than the average value. Figure 12d plots the normalized X-ray attenuation profile by averaging gray scales along the core sample's axis. These observations from Figure 12c and Figure ***12***d indicate that a higher level of precipitation occurred at the top and bottom sections of the rock sample, a result that agrees with the observations shown in Figure 11 for the X-ray data acquired at the Paul Scherrer Institute.

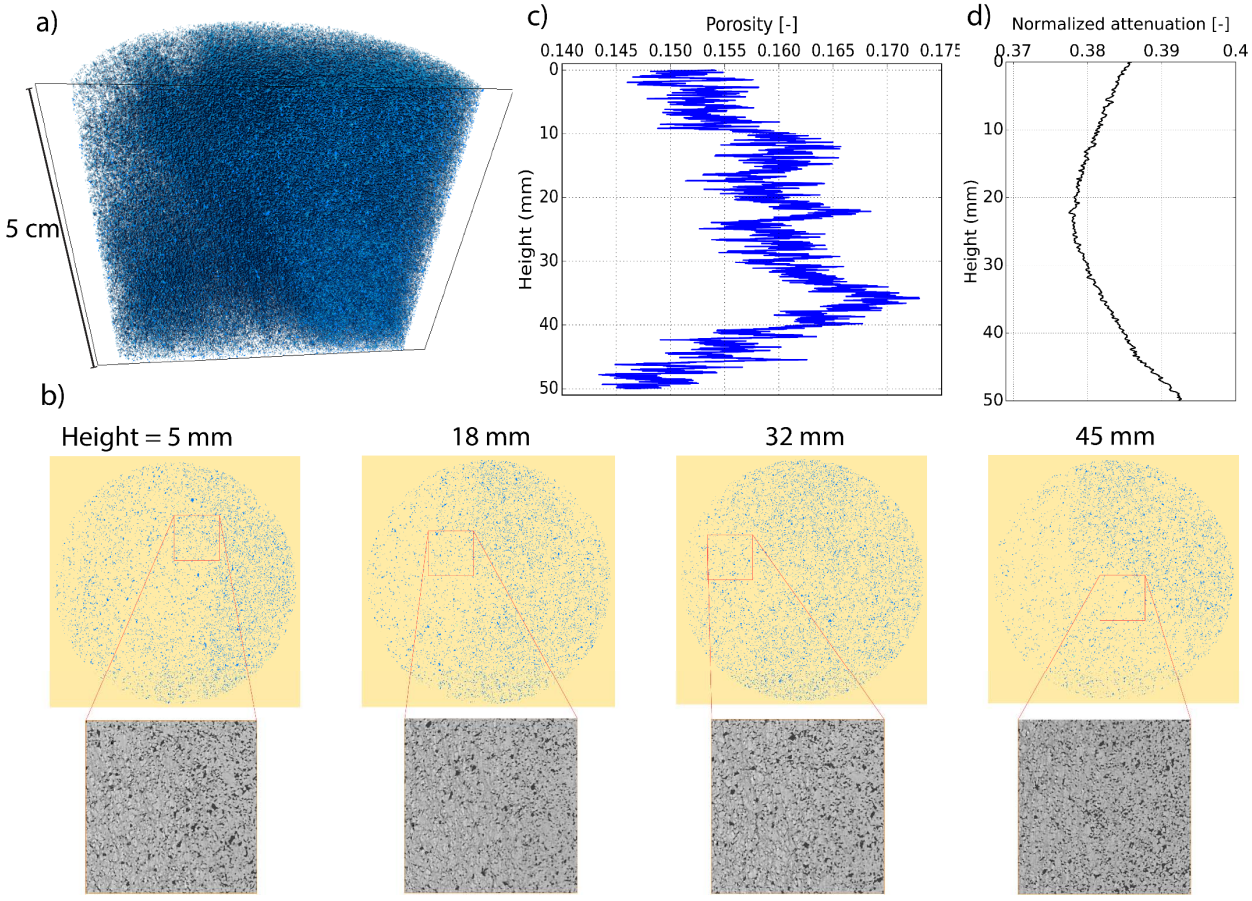

Figure 12: a) Rendering of the X-ray tomogram of sample BS2 acquired at the European Synchrotron Radiation Facility, with a voxel size of 5.85 micrometers. Pores are shown in blue. **b)** Two-dimensional slices of porosity distribution perpendicular to the core axis at different heights including X-ray tomograph zooms of small squares, where empty pores appear in black. **c)** Profile of porosity distribution along the axis of the core sample calculated by segmentation of the pores (sum of segmented pores divided by slice area), as shown in panel a). **d)** Normalized X-ray attenuation profile calculated by averaging gray values along the axis of the core sample.

4. Discussion

4.1 Neutron imaging of fluid flow in porous media

Neutron imaging has developed rapidly in the past few years, providing new opportunities for non-destructive characterization of a wide range of geomaterials (e.g., Tengattini et al., 2021). Several recent studies have demonstrated the capabilities of dynamic neutron imaging to study fluid flow in rocks, for example, to reveal the relationship between wormhole advancement and permeability variation in dissolving rocks (Cooper et al., 2023), or to investigate the interactions between imbibition and pressure-driven flow in microporous deformed limestone (Lewis et al., 2023). Neutron imaging has also been used to study transport properties in other porous media, such as the migration of condensed water vapor through cracked concrete (Gupta et al., 2022), hydrochannel porous transport layer designed for unitized reversible fuel cells (Komini Babu et al., 2023), as well as salt precipitation and water transport in CO_2 electrolysis (Disch et al., 2022). These studies demonstrate the versatility of the neutron imaging technique and its ability to provide a deeper understanding of fluid transport in various porous media.

The distinctive characteristics of a neutron beam, such as its isotope sensitivity (e.g., D_2O/H_2O) or its strong attenuation in the presence of cadmium, make neutron imaging a useful technique to study fluid flow and contaminant transport in porous rock. Heavy water (D_2O) exhibits significantly reduced neutron attenuation compared to regular water (H_2O), allowing for the investigation of fluid flow dynamics. Recent advances in neutron tomography techniques have facilitated quicker imaging and enabled scientists to capture fluid dynamics with enhanced spatial and temporal resolution. As an example, the CONRAD-2 neutron source (Helmholtz-Zentrum, Berlin) enables the monitoring of fluid front movement in saturated samples by utilizing the distinctive contrast in neutron attenuation (Etxegarai et al., 2021). The Institut Laue-Langevin in Grenoble, France is a neutron source where high-speed neutron tomographies with a rapid acquisition time of around one minute have been obtained to study water invasion into air-filled samples of rock (Tudisco et al., 2019). The neutron source SINQ at the Paul Scherrer Institute in Switzerland is another facility where we show in the present study the capability of in situ analysis of the local changes in fluid flow properties of rocks, expanding the possibilities for studying fluid dynamics in rock samples (Cordonnier et al., 2019). In the present study, we quantify the spatial fluctuations of fluid velocity before and after calcium carbonate precipitation in porous sandstone. We solved the inverse advection-dispersion equation using the difference in neutron attenuation between two miscible fluids, a technique that to the best of our knowledge has not been previously explored. The resolution of neutron images implies that the fluid velocities correspond to average pore velocities, which do not resolve the velocity field inside pores.

4.2 Dispersion of solutes quantified by neutron imaging

Recent advancements in understanding transverse dispersion dynamics in natural rock media have been made using X-ray tomography to study the steady-state dispersion of solutes (Boon et al., 2017; Boon et al., 2016). The potential of utilizing neutron imaging to measure dispersion is evaluated in this study. In experiment BS0, the width of the mixing zone between the heavy

water and cadmium solutions increases from the top to the bottom of rock sample BS0, as expected, showing the applicability of the neutron imaging technique in exploring the transverse dispersion in rock. The derived value of the transverse dispersion coefficient was obtained by fitting Eq. 2 to the normalized attenuation curves (Figure 4c) collected at different heights in sample BS0 is $D_T = 1.3\times10^{-9} m^2 s^{-1}$. Assuming the medium is homogeneous and the flow rate is low (Pe = 0.5), the transverse dispersion would be close to the molecular diffusion. The value of the dispersion coefficient we calculate is within a factor two comparable to the diffusion coefficient of cadmium into water ($7\times10^{-10} m^2 s^{-1}$) published in other studies (Furukawa et al., 2007; Lide and Kehiaian, 1994).

4.3 Fluctuations of fluid velocity in sandstone before and after mineral precipitation

The injection steps of D_2O in experiments BS1 and BS2 produce a visible fluid front in the tomograms. The shape and velocity of this front change before and after mineral precipitation steps, indicating local modifications of porosity that we interpret to be related to the clogging of some pores by calcium carbonate precipitation. In both samples BS1 and BS2, the velocity distribution curves observed after a precipitation step in Figure 8a and Figure 9a exhibit a higher and broader range of velocities. This effect is more pronounced in experiment BS2, where a higher amount of calcium carbonate precipitation occurred following the co-injection of Na_2CO_3 and $CaCl_2$.

Our results suggest that non-uniform precipitates can readily form at the pore scale. The decrease in permeability is associated with a reduction in porosity (Reis, 1994), due to the decrease in the size of the pore throats. This decrease in permeability induces an increase in the average fluid velocity under conditions of imposed flow rate. The formation of new minerals may also result in the development of roughness in the pores (Noiriel et al., 2016), which, in turn, may lead to a reduction in fluid velocity near the grain surface. This reduction is controlled by both the location and size of the newly formed crystals. The impact of local precipitation on fluid velocity may have substantial implications for the hydrodynamics and transport of reactants and products in the vicinity of the fluid-rock interface (Steefel and Maher, 2009).

For both experiments BS1 and BS2, we observed fluid velocity increases in certain areas and decreases in other areas of the rock sample. This effect is related to the porosity reduction due to localized calcium carbonate precipitation. To quantify the velocity field, we first calculated the path-averaged velocity of D_2O transported by advection, and then, we added a dispersion term with the approximation described in Eq. 11. The derived values of the dispersion coefficients in samples BS1 and BS2 before precipitation. 5.6×10^{-11} m^2/s and 8.0×10^{-11} m^2/s (see Section 3.2), are smaller than the value of 1.3×10^{-9} m^2/s calculated for sample BS0. One possible explanation is the use of a smoothing Lagrange multiplier in the variational formulation (Eq. 6), which acts like a diffusion term (Liu and Shen, 2008). However, we have shown that varying the value of the Lagrange multiplier between 10 and 50 does not modify significantly the distribution of the velocities (Figure S1). Another explanation could be attributed to a bias in the three-dimensional volume reconstruction process, which may have arisen from the relatively long 32-minute temporal resolution between each scan, during which fluid flow was occurring

within the rock. These factors combined with the assumption of considering the constant dispersion coefficient throughout the injections have led to the underestimation of this coefficient in samples BS1 and BS2.

4.4 X-ray imaging of local calcium carbonate precipitation and porosity and comparison with neutron imaging

X-ray imaging has been used to investigate the precipitation of calcium carbonate and porosity distribution in rocks. One study has shown that X-ray micro-tomography can provide a detailed view of the morphology and distribution of calcite precipitates in fractured rocks (Aben et al., 2017). X-ray imaging has also been used to observe how calcite precipitation affects the permeability, porosity, and fluid flow in porous rocks (e.g., Hebert et al., 2015; Noiriel, 2015; Noiriel et al., 2016). In this study, X-ray tomography acquisition of the sample BS2 allowed us to verify that calcite precipitation occurred in the rock and have a general estimation of its distribution. However, these X-rays cannot be used to explain the flow distribution since the unconsolidated precipitate likely moved in the pore space between the neutron and X-ray scans. Figure 13 presents vertical cross-sections of the sandstone samples acquired using different imaging methods. Figure 13a shows a section obtained using neutron imaging, which, despite its lower resolution, provides valuable insights to image the solutions present within the samples. Figure 13b and Figure 13c display sections acquired using low and high-resolution X-ray imaging. Notably, the high-resolution X-ray imaging provides enhanced visualization of the pore space and calcite distribution within the sample. At the pore scale, calcite-filled pores can be identified. As discussed above, it is not yet possible to fully connect the three-dimensional X-ray image with the three-dimensional velocity field obtained from the neutron tomogram series in order to determine the relationship between mineral precipitation and the fluid velocity at that region. Developing imaging techniques to allow for such developments should be the topic of future studies.

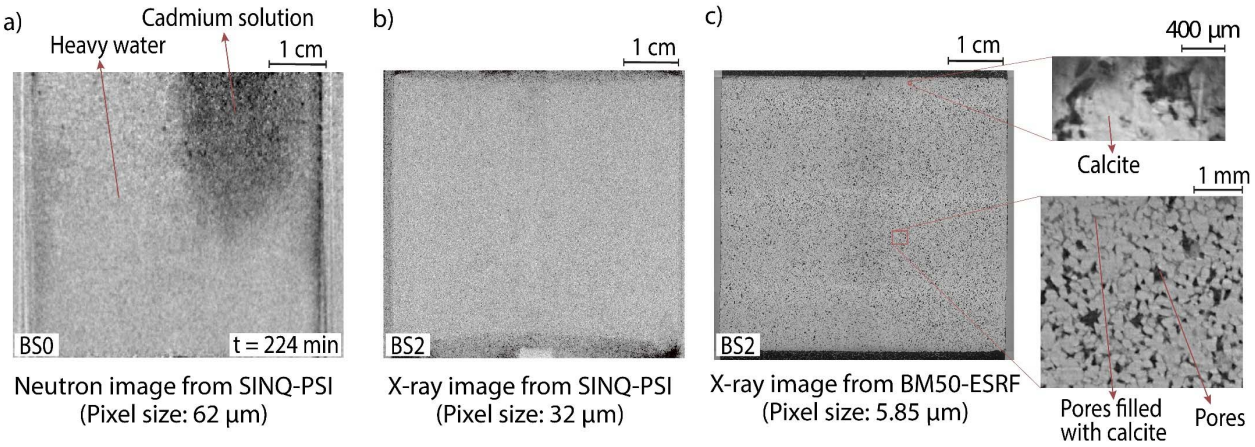

Figure 13. Vertical cross-sections of porous sandstone acquired using **a)** neutron imaging (sample BS0), **b)** low-resolution X-ray imaging (sample BS2), and **c)** high-resolution X-ray imaging (sample BS2).

5. Conclusions

This study uses dynamic neutron imaging to investigate flow and transport before and after mineral precipitation in core samples of Bentheim sandstone. Neutron imaging is shown to be a useful tool to track the transport of solute fronts in porous rocks since the rock and sample holder are mostly transparent to neutrons, whereas the aqueous fluid can be imaged under in situ conditions.

Hence, we investigated the feasibility and precision of neutron imaging to measure transverse solute dispersion induced by flow in porous rock. Furthermore, neutron imaging was used to visualize the flow of two aqueous miscible fluids within porous rock and its alteration by calcium carbonate precipitation. We developed an inverse method that uses the advection-dispersion equation to quantify the spatial fluctuations of the velocity of injected fluid by tracking the moving interface between two miscible fluids. While this technique did not provide pore-scale resolution, it was useful to monitor the distribution of the average pore velocity within the rock. After precipitation, the average velocity was larger and the flow field was more heterogeneous. This effect was more pronounced in the co-flow experiment compared to the sequential experiment. In the former, larger initial velocity tended to increase, explaining the broadening of the velocity distribution. X-ray imaging at different resolutions allowed us to confirm the presence of calcite precipitate inside the rock and estimate its spatial distribution in the rock. However, the transport of unconsolidated precipitate between the neutron and X-ray scan did not allow a direct correlation between the flow and precipitation fields. This could be achieved in the future by optimizing the coupling of neutron and X-ray imaging sequences.

These findings therefore open new opportunities to use neutron imaging, coupled with other tomography techniques, to investigate flow, transport, and reaction processes in porous media. Our results suggest an interesting coupling between flow and precipitation, particularly in the co-flow experiment. Following this proof of concept, the technique could be largely improved by better controlling the injection of reactive fluids, investigating reactive transport regimes where the precipitate is not transported, and optimizing the coupling of neutron and X-ray imaging.

Acknowledgments. The study received funding from the Akademiaavtalen (Academic Agreement) between Equinor and the University of Oslo through the project MODIFLOW. This work is based on experiments performed at the Swiss spallation neutron source SINQ, Paul Scherrer Institute, Villigen, Switzerland.

Data availability statement. The data and the codes supporting the results in this manuscript are available in Shafabakhsh (2023) [Dataset].

References

Aben, F., Doan, M.L., Gratier, J.P. and Renard, F. 2017. Experimental postseismic recovery of fractured rocks assisted by calcite sealing. Geophysical Research Letters 44(14), 7228-7238.

649 Anderson, I.S., McGreevy, R.L. and Bilheux, H.Z. 2009. Neutron imaging and applications.
650 Springer Science+Business Media 200(2209), 987-980.
651 Andrew, M., Menke, H., Blunt, M.J. and Bijeljic, B. 2015. The imaging of dynamic multiphase
652 fluid flow using synchrotron-based X-ray microtomography at reservoir conditions.
653 Transport in Porous Media 110(1), 1-24.
654 Balog, E., Bittmann, K., Schwarzenberger, K., Eckert, K., De Wit, A. and Schuszter, G. 2019.
655 Influence of microscopic precipitate structures on macroscopic pattern formation in reactive
656 flows in a confined geometry. Physical Chemistry Chemical Physics 21(6), 2910-2918.
657 Baqer, Y. and Chen, X. 2022. A review on reactive transport model and porosity evolution in the
658 porous media. Environmental Science and Pollution Research 29(32), 47873–47901.
659 Beckingham, L.E. 2017. Evaluation of macroscopic porosity-permeability relationships in
660 heterogeneous mineral dissolution and precipitation scenarios. Water Resources Research
661 53(12), 10217-10230.
662 Boon, M., Bijeljic, B. and Krevor, S. 2017. Observations of the impact of rock heterogeneity on
663 solute spreading and mixing. Water Resources Research 53(6), 4624-4642.
664 Boon, M., Bijeljic, B., Niu, B. and Krevor, S. 2016. Observations of 3-D transverse dispersion
665 and dilution in natural consolidated rock by X-ray tomography. Advances in Water
666 Resources 96, 266-281.
667 Bray, J.M., Lauchnor, E.G., Redden, G.D., Gerlach, R., Fujita, Y., Codd, S.L. and Seymour, J.D.
668 2017. Impact of mineral precipitation on flow and mixing in porous media determined by
669 microcomputed tomography and MRI. Environmental Science Technology and Health Care
670 51(3), 1562-1569.
671 Brečević, L. and Nielsen, A.E. 1989. Solubility of amorphous calcium carbonate. Journal of
672 Crystal Growth 98(3), 504-510.
673 Chang, R., Kim, S., Lee, S., Choi, S., Kim, M. and Park, Y. 2017. Calcium carbonate
674 precipitation for CO2 storage and utilization: a review of the carbonate crystallization and
675 polymorphism. Frontiers in Energy Research 5, 17.
676 Cooper, M.P., Sharma, R.P., Magni, S., Blach, T.P., Radlinski, A.P., Drabik, K., Tengattini, A.
677 and Szymczak, P. 2023. 4D tomography reveals a complex relationship between wormhole
678 advancement and permeability variation in dissolving rocks. Advances in Water Resources
679 175, 104407.
680 Cordonnier, B., Pluymakers, A., Tengattini, A., Marti, S., Kaestner, A., Fusseis, F. and Renard,
681 F. 2019. Neutron imaging of cadmium sorption and transport in porous rocks. Frontiers in
682 Earth sciences 7, 306.
683 Dávila, G., Dalton, L., Crandall, D.M., Garing, C., Werth, C.J. and Druhan, J.L. 2020. Reactive
684 alteration of a Mt. Simon Sandstone due to CO2-rich brine displacement. Geochimica et
685 Cosmochimica Acta 271, 227-247.
686 Desrues, J., Viggiani, G. and Besuelle, P. (2010) Advances in X-ray Tomography for
687 Geomaterials, John Wiley & Sons.
688 Disch, J., Bohn, L., Koch, S., Schulz, M., Han, Y., Tengattini, A., Helfen, L., Breitwieser, M.
689 and Vierrath, S. 2022. High-resolution neutron imaging of salt precipitation and water
690 transport in zero-gap CO2 electrolysis. Nature Communications 13(1), 6099.
691 Ebigbo, A., Phillips, A., Gerlach, R., Helmig, R., Cunningham, A.B., Class, H. and Spangler,
692 L.H. 2012. Darcy-scale modeling of microbially induced carbonate mineral precipitation in
693 sand columns. Water Resources Research 48(7), 1-17.

694 Emmanuel, S. and Berkowitz, B. 2005. Mixing-induced precipitation and porosity evolution in
695 porous media. Advances in Water Resources 28(4), 337-344.
696 Eriksson, N. and Destouni, G. 1997. Combined effects of dissolution kinetics, secondary mineral
697 precipitation, and preferential flow on copper leaching from mining waste rock. Water
698 Resources Research 33(3), 471-483.
699 Etxegarai, M., Tudisco, E., Tengattini, A., Viggiani, G., Kardjilov, N. and Hall, S.A. 2021.
700 Characterisation of single-phase fluid-flow heterogeneity due to localised deformation in a
701 porous rock using rapid neutron tomography. Journal of Imaging 7(12), 275.
702 Fisher, Q. and Knipe, R. 1998. Fault sealing processes in siliciclastic sediments. Geological
703 Society, London, Special Publications 147(1), 117-134.
704 Furukawa, K., Takahashi, Y. and Sato, H. 2007. Effect of the formation of EDTA complexes on
705 the diffusion of metal ions in water. Geochimica et Cosmochimica Acta 71(18), 4416-4424.
706 Garing, C., Gouze, P., Kassab, M., Riva, M. and Guadagnini, A. 2015. Anti-correlated porosity–
707 permeability changes during the dissolution of carbonate rocks: experimental evidences and
708 modeling. Transport in Porous Media 107(2), 595-621.
709 Gautschi, W. and Cahill, W. 1964. Handbook of mathematical functions. Abramowitz IA Stegun
710 eds., National Bureau of Standards, Washington DC.
711 Godinho, J.R., Gerke, K.M., Stack, A.G. and Lee, P.D. 2016. The dynamic nature of crystal
712 growth in pores. Scientific Reports 6(1), 33086.
713 Gupta, R., Lukić, B., Tengattini, A., Dufour, F. and Briffaut, M. 2022. Experimental
714 characterisation of transient condensed water vapour migration through cracked concrete as
715 revealed by neutron and x-ray imaging: Effect of initial saturation. Cement Concrete
716 Research 162, 106987.
717 Hebert, V., Garing, C., Luquot, L., Pezard, P. and Gouze, P. 2015. Multi-scale X-ray tomography
718 analysis of carbonate porosity. Geological Society, London, Special Publications 406(1), 61-
719 79.
720 Hoefner, M. and Fogler, H.S. 1988. Pore evolution and channel formation during flow and
721 reaction in porous media. AICHE Journal 34(1), 45-54.
722 Hommel, J., Coltman, E. and Class, H. 2018. Porosity–permeability relations for evolving pore
723 space: a review with a focus on (bio-) geochemically altered porous media. Transport in
724 Porous Media 124(2), 589-629.
725 Horn, B.K. and Schunck, B.G. 1981. Determining optical flow. Artificial Intelligence in
726 Medicine 17(1-3), 185-203.
727 Izumoto, S., Huisman, J.A., Zimmermann, E., Heyman, J., Gomez, F., Tabuteau, H., Laniel, R.,
728 Vereecken, H., Méheust, Y. and Le Borgne, T. 2022. Pore-scale mechanisms for spectral
729 induced polarization of calcite precipitation inferred from geo-electrical millifluidics.
730 Environmental Science Technology 56(8), 4998-5008.
731 Kaestner, A., Hartmann, S., Kühne, G., Frei, G., Grünzweig, C., Josic, L., Schmid, F. and
732 Lehmann, E.J. 2011. The ICON beamline–A facility for cold neutron imaging at SINQ.
733 Nuclear Instruments Methods in Physics Research Section A: Accelerators, Spectrometers,
734 Detectors Associated Equipment 659(1), 387-393.
735 Kaestner, A., Hassanein, R., Vontobel, P., Lehmann, P., Schaap, J., Lehmann, E. and Flühler, H.
736 2007. Mapping the 3D water dynamics in heterogeneous sands using thermal neutrons.
737 Chemical Engineering Journal 130(2-3), 79-85.

738 Kaestner, A., Hovind, J., Boillat, P., Muehlebach, C., Carminati, C., Zarebanadkouki, M. and
739 Lehmann, E.H. 2017. Bimodal imaging at ICON using neutrons and X-rays. Physics
740 Procedia 88, 314-321.
741 Kaestner, A.P. 2011. MuhRec—A new tomography reconstructor. Nuclear Instruments Methods
742 in Physics Research Section A: Accelerators, Spectrometers, Detectors Associated
743 Equipment 651(1), 156-160.
744 Kim, F.H., Penumadu, D., Gregor, J., Kardjilov, N. and Manke, I. 2013. High-resolution neutron
745 and X-ray imaging of granular materials. Journal of Geotechnical Geoenvironmental
746 Engineering 139(5), 715-723.
747 Klein, E., Baud, P., Reuschlé, T. and Wong, T. 2001. Mechanical behaviour and failure mode of
748 Bentheim sandstone under triaxial compression. Physics Chemistry of the Earth, Part A:
749 Solid Earth Geodesy 26(1-2), 21-25.
750 Komini Babu, S., Yilmaz, A., Uddin, M.A., LaManna, J., Baltic, E., Jacobson, D.L.,
751 Pasaogullari, U. and Spendelow, J.S. 2023. A Goldilocks Approach to Water Management:
752 Hydrochannel Porous Transport Layers for Unitized Reversible Fuel Cells. Advanced
753 Energy Materials 13(16), 2203952.
754 Kudrolli, A. and Clotet, X. 2016. Evolution of porosity and channelization of an erosive medium
755 driven by fluid flow. Physical Review Letters 117(2), 028001.
756 Lewis, H., Couples, G., Tengattini, A., Buckman, J., Tudisco, E., Etxegarai, M., Viggiani, G. and
757 Hall, S.A. 2023. Interactions Between Imbibition and Pressure-Driven Flow in a
758 Microporous Deformed Limestone. Transport in Porous Media 146(3), 559-585.
759 Lichtner, P.C. 1996. Continuum formulation of multicomponent-multiphase reactive transport.
760 Reviews in Mineralogy and Geochemistry 34, 1-82.
761 Lide, D.R. and Kehiaian, H.V. (1994) CRC handbook of thermophysical and thermochemical
762 data, CRC press.
763 Liu, T. 2017. OpenOpticalFlow: An open source program for extraction of velocity fields from
764 flow visualization images. Journal of Open Research Software 5(1), 29.
765 Liu, T. and Shen, L. 2008. Fluid flow and optical flow. Journal of Fluid Mechanics 614, 253-
766 291.
767 Mancini, L., Arzilli, F., Polacci, M. and Voltolini, M. 2020. Recent Advancements in X-Ray and
768 Neutron Imaging of Dynamic Processes in Earth Sciences. Frontiers in Earth Sciences 8,
769 588463.
770 Mitchell, A.C., Espinosa-Ortiz, E.J., Parks, S.L., Phillips, A.J., Cunningham, A.B. and Gerlach,
771 R. 2019. Kinetics of calcite precipitation by ureolytic bacteria under aerobic and anaerobic
772 conditions. Biogeosciences Discussions 16(10), 2147-2161.
773 Morse, J.W., Arvidson, R.S. and Lüttge, A. 2007. Calcium carbonate formation and dissolution.
774 Chemical Reviews (Washington, D. C.) 107(2), 342-381.
775 Mujah, D., Shahin, M.A. and Cheng, L. 2017. State-of-the-art review of biocementation by
776 microbially induced calcite precipitation (MICP) for soil stabilization. Geomicrobiology
777 Journal 34(6), 524-537.
778 Noiriel, C. 2015. Resolving time-dependent evolution of pore-scale structure, permeability and
779 reactivity using X-ray microtomography. Reviews in Mineralogy Geochemistry and the
780 Environment 80(1), 247-285.
781 Noiriel, C., Seigneur, N., Le Guern, P. and Lagneau, V. 2021. Geometry and mineral
782 heterogeneity controls on precipitation in fractures: An X-ray micro-tomography and
783 reactive transport modeling study. Advances in Water Resources 152, 103916.

784 Noiriel, C. and Soulaine, C. 2021. Pore-scale imaging and modelling of reactive flow in evolving
785 porous media: Tracking the dynamics of the fluid–rock interface. Transport in Porous Media
786 140(1), 181-213.
787 Noiriel, C., Steefel, C.I., Yang, L. and Ajo-Franklin, J. 2012. Upscaling calcium carbonate
788 precipitation rates from pore to continuum scale. Chemical Geology 318, 60-74.
789 Noiriel, C., Steefel, C.I., Yang, L. and Bernard, D. 2016. Effects of pore-scale precipitation on
790 permeability and flow. Advances in Water Resources 95, 125-137.
791 Perfect, E., Cheng, C.-L., Kang, M., Bilheux, H., Lamanna, J., Gragg, M. and Wright, D. 2014.
792 Neutron imaging of hydrogen-rich fluids in geomaterials and engineered porous media: A
793 review. Earth-Science Reviews 129, 120-135.
794 Plummer, L., Parkhurst, D. and Wigley, T. 1979. Critical review of the kinetics of calcite
795 dissolution and precipitation. ACS Symposium Series 93, 537-573.
796 Reis, J.A., AM 1994. Permeability reduction models for the precipitation of inorganic solids in
797 Berea sandstone. In situ 18(3), 347-368.
798 Renard, F., Bernard, D., Thibault, X. and Boller, E. 2004. Synchrotron 3D microtomography of
799 halite aggregates during experimental pressure solution creep and evolution of the
800 permeability. Geophysical Research Letters 31(7).
801 Sabo, M.S. and Beckingham, L.E. 2021. Porosity-Permeability Evolution During Simultaneous
802 Mineral Dissolution and Precipitation. Water Resources Research 57(6), e2020WR029072.
803 Scanziani, A., Alhosani, A., Lin, Q., Spurin, C., Garfi, G., Blunt, M.J. and Bijeljic, B. 2020. In
804 situ characterization of three-phase flow in mixed-wet porous media using synchrotron
805 imaging. Water Resources Research 56(9), e2020WR027873.
806 Schuszter, G., Brau, F. and De Wit, A. 2016. Flow-driven control of calcium carbonate
807 precipitation patterns in a confined geometry. Physical Chemistry Chemical Physics 18(36),
808 25592-25600.
809 Seigneur, N., Mayer, K.U. and Steefel, C.I. 2019. Reactive transport in evolving porous media.
810 Reviews in Mineralogy Geochemistry and the Environment 85(1), 197-238.
811 Shafabakhsh, P. 2023. Dynamic neutron imaging of solute transport and fluid flow in sandstone
812 before and after mineral precipitation [Data set]. https://doi.org/10.11582/2023.00109.
813 Simmons, S.F. and Christenson, B.W. 1994. Origins of calcite in a boiling geothermal system.
814 American Journal of Science 294(3), 361-400.
815 Steefel, C.I. and Lasaga, A.C. (1990) Evolution of dissolution patterns: Permeability change due
816 to coupled flow and reaction, pp. 212-225, ACS Publications.
817 Steefel, C.I. and Maher, K. 2009. Fluid-rock interaction: A reactive transport approach. Reviews
818 in mineralogy geochemistry and the Environment 70(1), 485-532.
819 Swinehart, D.F. 1962. The Beer-Lambert law. Journal of Chemical Education 39(7), 333-335.
820 Tengattini, A., Lenoir, N., Ando, E. and Viggiani, G. 2021. Neutron imaging for geomechanics:
821 A review. Geomechanics for Energy the Environment 27, 100206.
822 Thullner, M., Zeyer, J. and Kinzelbach, W. 2002. Influence of microbial growth on hydraulic
823 properties of pore networks. Transport in porous media 49(1), 99-122.
824 Tötzke, C., Manke, I., Hilger, A., Choinka, G., Kardjilov, N., Arlt, T., Markötter, H., Schröder,
825 A., Wippermann, K. and Stolten, D. 2011. Large area high resolution neutron imaging
826 detector for fuel cell research. Journal of Power Sources 196(10), 4631-4637.
827 Tudisco, E., Etxegarai, M., Hall, S.A., Charalampidou, E.M., Couples, G.D., Lewis, H.,
828 Tengattini, A. and Kardjilov, N. 2019. Fast 4-D Imaging of Fluid Flow in Rock by High-

Speed Neutron Tomography. Journal of Geophysical Research: Solid Earth 124(4), 3557-3569.

Vinegar, H. 1986. X-ray CT and NMR imaging of rocks. Journal of Petroleum Technology 38(03), 257-259.

Wu, J., Wang, X.-B., Wang, H.-F. and Zeng, R.J. 2017. Microbially induced calcium carbonate precipitation driven by ureolysis to enhance oil recovery. RSC advances 7(59), 37382-37391.

Zhang, Y. and Dawe, R. 1998. The kinetics of calcite precipitation from a high salinity water. Applied Geochemistry 13(2), 177-184.